Main Manuscript for

Interactions among Diameter, Myelination and the Na/K pump Affect Axonal Resilience to High Frequency Spiking

Yunliang Zang & Eve Marder*

Volen Center and Department of Biology, Brandeis University, Waltham, MA 02454, USA

*Eve Marder

Email: marder@brandeis.edu

Author Contributions: YZ and EM designed this research; YZ implemented model building, model simulation, data analysis, figure generation; YZ and EM wrote and revised the manuscript.

Competing Interest Statement: The authors declare no competing financial interests

Classification: Major - Biological Sciences; minor - Neuroscience

Keywords: computational model; action potential; node of Ranvier; electrogenic pumps; sodium dynamics

This PDF file includes:

Main Text

Figures 1 to 4

Abstract

Axons reliably conduct action potentials between neurons and/or other targets. Axons have widely variable diameters and can be myelinated or unmyelinated. Although the effect of these factors on propagation speed is well studied, how they constrain axonal resilience to high frequency spiking is incompletely understood. Maximal firing frequencies range from ~ 1 Hz to > 300 Hz across neurons, but the process by which Na/K pumps counteract Na^+ influx is slow, and it is unclear the extent to which slow Na^+ removal is compatible with high frequency spiking. Modeling the process of Na^+ removal shows that large diameter axons are more resilient to high frequency spikes than small diameter axons, because of their slow Na^+ accumulation. In myelinated axons, the myelinated compartments between nodes of Ranvier act as a 'reservoir' to slow Na^+ accumulation and increase the reliability of axonal propagation. We now find that slowing the activation of K^+ current can increase the Na^+ influx rate, and the effect of minimizing the overlap between Na^+- and K^+-currents on spike propagation resilience depends on complex interactions among diameter, myelination and the Na/K pump density. Our results suggest that, in neurons with different channel gating kinetic parameters, different strategies may be required to improve the reliability of axonal propagation.

Significance Statement

The reliability of spike propagation in axons is determined by complex interactions among ionic currents, ion pumps and morphological properties. We use compartment-based modeling to reveal that interactions of diameter, myelination and the Na/K pump determine the reliability of high frequency spike propagation. By acting as a 'reservoir' of nodal Na^+ influx, myelinated compartments efficiently increase propagation reliability. Although spike broadening was thought to oppose fast spiking, its effect on spike propagation is complicated, depending on the balance of Na^+ channel inactivation gate recovery, Na^+ influx and axial charge. Our findings suggest that slow Na^+ removal influences axonal resilience to high frequency spike propagation, and that different strategies may be required to overcome this constraint in different neurons.

Main Text

Introduction

Axons usually reliably conduct information (spikes) to other neurons, muscles and glands. The largest diameter axons are found in some invertebrates, where the squid giant axon and arthropod giant fibers are parts of rapid escape systems. In the mammalian nervous system, axon diameters can differ by a factor of > 100. Some are covered with myelin sheaths but others are not (1). Both myelination and large axon diameter increase spike propagation speed (2, 3), and the latter factor can also increase axonal resilience to noise perturbation (4).

Neuronal firing frequency is not static, but variations in firing rates are used to encode a wide range of signals such as inputs from sensory organs and command signals from motor cortex. The maximal firing frequency, critical for neuronal functional capacity, ranges from ~ 1 Hz to > 300 Hz (5-8). However, it remains unclear how axonal physical properties constrain axonal resilience to high frequency firing. During action potentials, Na^+ flows into axons and then ATP is used by Na/K pumps to pump out the excess Na^+. Given the limited energy supply in the brain, evolutionary strategies including shortening spike propagation distance, sparse coding and reducing Na^+- and K^+-current overlap etc. have helped minimize energy expenditure (9-13). However, the observation that high frequency spiking tends to occur in large diameter axons (5) is confusing because fast spiking in large diameter axons causes more Na^+ influx and exerts a heavy burden on the energy supply in the brain (14, 15). Additionally, the process by which Na/K pumps remove Na^+ is slow (16-22). In neurons, it takes seconds or even minutes to remove the excess Na^+ after $[Na^+]$ elevation (16-21). It remains unknown how these directly correlated processes, fast spiking and slow Na^+ removal, interact in the control of reliable spike generation

and propagation. Furthermore, it is unclear whether reducing Na^+- and K^+-current overlap can consistently decrease the rate of Na^+ influx and accordingly enhance axonal reliability to propagate high frequency spikes. Consequently, by modeling the process of Na^+ removal in unmyelinated and myelinated axons, we systematically explored the effects of diameter, myelination and Na/K pump density on spike propagation reliability.

Results

Different [Na^+] Decay Dynamics in Unmyelinated and Myelinated Axons. We implemented multicompartment models of axons in NEURON (23). Both the unmyelinated and myelinated axon models include I_{Na}, I_{KD}, I_{KA}, I_{leak} and the Na/K pump. All channels and pumps were evenly spread in the unmyelinated axon model and at the nodes of Ranvier in the myelinated axon model. For the myelinated compartments, there is a significantly lower density of I_{leak} and C_m to simulate the effect of insulation (Materials and Methods). The model structures are shown in Fig. 1A.

Spikes propagate rapidly in both models. In the unmyelinated axon model, the propagation increases from 0.1 m/s to 0.3 m/s when the axonal diameter increases from 0.2 μm to 1 μm. In the myelinated axon model, the speed increases from 0.87 m/s to 2.1 m/s accordingly. Upon the arrival of spikes, Na^+ channels open and extracellular Na^+ flows into axons to raise the intracellular [Na^+] immediately (Fig. 1B). Then K^+ currents are activated to repolarize the spikes. Compared with the other ionic currents, the magnitude of the Na/K pump current is extremely small during a single spike, but it decays very slowly. Eventually, the Na/K pump gradually removes Na^+ from the axon, leading to a slow, many second, [Na^+] decay in the unmyelinated axon model (Fig. 1B, left). In contrast, in the myelinated axon model, the spike-triggered [Na^+] elevation at the node of Ranvier decays on the time scale of hundreds of ms (Fig. 1B, right). The Na/K pump densities in the two

models are the same and thus the quick decay is not a result of super-efficient pumps. In the myelinated axon model, Na^+ channels are placed only in the nodes of Ranvier and there is no transmembrane Na^+ influx in the myelinated compartments. But, the slightly elevated [Na^+] in the myelinated compartment and the rapid decay of nodal [Na^+] are due to the axial diffusion of Na^+ into neighboring myelinated compartments, rather than immediate pump action.

Because of the large diffusion coefficient (24) and the lack of buffering (16), [Na^+] in the radial direction becomes rapidly homogeneous. Thus, spike-triggered [Na^+] elevation can be well predicted by the surface-to-volume ratio (SVR $\propto$ 1/diameter). In both models, spike-triggered [Na^+] elevation decreases with diameter (Fig. 1C). Increasing the pump density speeds up the [Na^+] decay in the unmyelinated axon model, but has no obvious effect on the nodal [Na^+] decay in the myelinated axon model, further confirming that the quick decay is not a result of the Na/K pump.

Na^+ Accumulation in the Unmyelinated Axon at High Firing Frequencies. Compared with the basal level before spiking (~ 10 mM), the [Na^+] elevation caused by a single spike is small and insufficient to affect axonal excitability (Fig. 1B). However, neurons can fire at high frequencies in certain behavioral contexts (7, 25-27). With continuous high frequency spiking, Na^+ can accumulate if subsequent spikes occur before the complete recovery of a preceding spike elicited [Na^+] rise. In the unmyelinated axon model, Na^+ significantly accumulates within just 100 spikes, and the accumulation speed increases with firing frequency because of a faster Na^+ influx rate (Fig. 2A). Larger SVRs can also make Na^+ accumulate faster in thin axons. Note that the seemingly slower Na^+ accumulation in the 0.2-μm-diameter axon at 60 Hz is due to earlier propagation failure. In parallel with Na^+ accumulation, the Na^+ equilibrium potential (driving force of Na^+ current) becomes more negative and the action potential peak decreases (Fig. 2B, C). With increased firing

frequency, propagation starts to fail. The failure starts from 30 Hz in the 0.2-μm-diameter axon (Fig. 2C), but from 60 Hz in larger diameter axons. A repertoire of propagation failure patterns were observed. In Fig. 2D1, every other spike propagated through the axon, but a more complicated propagation failure pattern is shown in Fig. 2D2.

When the model fires over a sufficiently long period, the Na^+ influx rate and efflux rate gradually balance each other to make [Na^+] reach a steady state. Despite different accumulation speeds, the steady state [Na^+] increases with firing frequency and is independent of diameter until propagation starts to fail (Fig. 2E). The rate of Na^+ influx per surface area is only determined by the firing frequency because of identical Na^+ channel density. The Na/K pump-caused net Na^+ efflux rate is determined by $-3k_1[pump][Na^+]^3 + 3k_2[pumpNa]$. Because the pump density is also identical, the model needs identical [Na^+] to match influx rate and reach a steady state irrespective of diameters. If propagation fails, the steady state [Na^+] depends on the actual pattern of spikes that propagate through the axon. For example, at 70 Hz with baseline pump density, the steady state [Na^+] is the same in the 0.6- and 1.0-μm-diameter axons but lower in the 0.2-μm-diameter axon, because of their specific propagation failure patterns (Fig. 2E). When pumps remove excess Na^+, they also carry a negative current, which gradually repolarizes the membrane potential during spikes along with Na^+ accumulation. The factors causing the gradual occurrence of failure includes the Na^+ channel's incomplete recovery from inactivation, decreased driving force due to Na^+ accumulation, and increased outward pump current during continuous spiking. This propagation failure can be eliminated or alleviated when Na^+ accumulation is not considered in the model. Increasing pump density consistently reduces Na^+ accumulation (Fig. 2E) to alleviate the equilibrium potential decrease, but also enhances the outward pump current to directly decrease the axonal excitability (Fig. 2F).

140 Na^+ accumulates slowly in large diameter axons and in these axons it always requires more
141 spikes to trigger propagation failure than in small diameter axons, making these axons more
142 resilient to high frequency firing (Fig. 2G). At higher frequencies, Na^+ accumulates faster and Na^+
143 channels recover less from inactivation. Consequently, fewer spikes are required to trigger
144 propagation failure and accordingly the resilience decreases (Fig. 2G). With higher pump densities
145 in the model, the axonal resilience to high frequency spiking is increased (Fig. 2 G), suggesting
146 that the alleviated decrease in Na^+ equilibrium potential prevails against the enhanced outward
147 pump current (Fig. 2F).

148 **Myelinated Compartments Slow Na^+ Accumulation.** In contrast to the slow decay of [Na^+] in
149 the unmyelinated axon, the [Na^+] at the node of Ranvier in the myelinated axon shows a quick
150 decay (Fig. 1B). Can nodal [Na^+] elevate at high firing frequencies? It does elevate to reduce the
151 Na^+ equilibrium potential and action potential peak in parallel (Fig. 3A-C). As explained
152 previously, the quick decay of nodal [Na^+] is a result of nodal Na^+ quickly diffusing into
153 neighboring myelinated compartments rather than being removed. After diffusion, the nodal [Na^+]
154 is still higher than the pre-spiking level (Fig. 1B). In other words, nodal Na^+ influx not only needs
155 to fill the nodes of Ranvier, but also the neighboring myelinated compartments, which is equivalent
156 to decreasing the SVR. Consequently, the nodal Na^+ still accumulates, but at a much slower rate
157 (Fig. 3A, F). It requires thousands of spikes to significantly change nodal [Na^+] in myelinated
158 axons. Na^+ in the myelinated compartments flows back during the removal of Na^+ by nodal Na/K
159 pumps. Therefore, by acting like an 'anti-flood water reservoir', myelinated compartments slow
160 down the nodal Na^+ accumulation and the excitability reduction.

161 Similar to the case in unmyelinated axon models, nodal Na^+ accumulates faster at higher firing
162 frequencies (Fig, 3A). Propagation failure starts from 50 Hz in the 0.2-μm-diameter axon, but from

163 60 Hz in larger diameter axons. In Fig. 3D1, every other spike can propagate through the axon.
164 However, only every fourth spike can successfully propagate in Fig. 3D2. The steady state [Na^+]
165 is diameter independent until propagation fails at high frequencies (Fig. 3E). When firing at 80 Hz
166 with baseline pump density, the steady state [Na^+] is still the same in axons with different diameters,
167 because they eventually have the same propagation patterns.

168 Because Na^+ accumulates more slowly in myelinated axons compared with unmyelinated axons
169 (Fig. 3F), the propagation is more reliable in myelinated axons (Fig. 3G). Large diameter axons
170 are consistently more resilient and the resilience decreases with firing frequency. Similar to
171 unmyelinated axon models, more pumps increase the propagation resilience.

172

173 **The Effects of Na^+-and K^+-Current Overlap on Propagation Resilience.** Previous work has
174 shown that the temporal overlap between the Na^+- and K^+-currents strongly affects Na^+ influx
175 during spiking (8). Can minimizing their temporal overlap consistently enhance axonal resilience
176 by reducing the rates of Na^+ influx and Na^+ accumulation?

177 Slowing the activation of I_{KD} was reported to increase spike duration and decrease Na^+ influx
178 per spike (8). However, slowing I_{KD} activation increases spike triggered Na^+ influx instead of
179 decreasing it in our model (Fig. 4A, c→d). By systematically varying I_{KD} activation time constant
180 in the range of 0.2-1.4 times of the baseline value, we observed a U-shaped relationship between
181 Na^+ influx rate and I_{KD} activation rate. Slowing the activation rate initially decreases the Na^+ influx
182 rate, but further slowing it increases the Na^+ influx rate (Fig. 4A). This occurs because slowing I_{KD}
183 activation increases spike duration to widen the Na^+ current profile; on the other hand, slower
184 repolarization reduces the Na^+ channel driving force to decrease the current amplitude during the

185 repolarization phase. Their balance determines the net change of Na^+ influx rate caused by slowing
186 the I_{KD} activation.

187 Apart from the U-shaped Na^+ influx rate changes, slowing I_{KD} activation consistently increases
188 spike duration, which results in changes that both favor and oppose spike propagation. Broader
189 spikes provide more axial charge to neighboring segments per spike to favor spike propagation,
190 but they also cause larger Na^+ channel inactivation and less recovery to oppose spiking. These
191 factors interact to make the effect of slowing I_{KD} activation on propagation reliability complex
192 (Fig. 4B, C). In both unmyelinated and myelinated axon models, slowing I_{KD} activation from a to
193 b consistently increases the propagation resilience. However, when slowing I_{KD} activation from b
194 to c, the resilience increases at low firing rates but decreases at high firing rates in both models.
195 Slowing I_{KD} activation from c to d consistently reduces the resilience in both models. These
196 complex effects reflect the interactions among Na^+ influx rate, spike duration and Na^+ channel
197 inactivation gate state changes.

198 We also explored the effect of speeding Na^+ current inactivation on propagation reliability.
199 Faster Na^+ current inactivation consistently reduces spike duration and Na^+ influx, but it also has
200 complex effects on the resilience because of the interactions among the above-mentioned opposing
201 factors (Fig. S1). The effects of diameter and myelination on the speed of Na^+ accumulation and
202 propagation resilience hold in all the simulations we have done.

203 Discussion

204 Neuronal firing frequency often varies over a broad range to encode a wide range of signals. For
205 a given neuron, the rate of Na^+ entry at its high firing frequency is usually much higher than the
206 rate at which excess Na^+ is pumped out of the cell. Therefore, while short periods of high frequency
207 firing should present no problem for most neurons, continuous high frequency spiking could result

208 in compromised function, as intracellular [Na^+] increases. Hence, we explore the dynamic
209 relationships between fast spiking and slow Na^+ removal for reliable spike generation and
210 propagation.

211 The importance of the Na/K ATPase in regulating neuronal activities has attracted attention in
212 recent years (28). It can set neuronal excitability and contribute to maintaining synchronous
213 epileptiform bursting in developing CA3 neurons (29). By interacting with h-current, it regulates
214 bursting activity in the leech heartbeat central pattern generator (30). There have also been
215 theoretical efforts to study the pump's role in controlling the transition between different firing
216 patterns (31-33) and the transition between normal and pathological brain states (34-37). However,
217 to the best of our knowledge, how the pump interacts with axon diameter and myelin to remove
218 Na^+ influx and affect axonal excitability has not been previously explored.

219 Axonal morphology can exert a critical constraint on a neuron's maximal firing frequency.
220 Large diameter and myelinated axons are intrinsically advantageous to propagate spikes because
221 of their larger space constants. In this work, we highlight another advantage in propagating
222 continuous high frequency spikes. Lower SVRs and slower Na^+ accumulation make them more
223 resilient to high frequency spiking. This may explain why fast-spiking parvalbumin interneurons
224 are extensively myelinated (38) and why high frequency spiking tends to occur in large diameter
225 axons, despite a higher energy cost of information transmission (5, 14, 15). Note that rapid
226 redistribution of ions such as Na^+ can occur at other sites and in other processes. For example, the
227 soma, acting as a Na^+ sink, can enhance reliable spike initiation in axon initial segments (16).
228 Redistribution of chloride in dendrites is also shown to be important for chloride equilibrium
229 potential and synaptic inhibition (39).

230 Increasing the Na/K pump density to remove Na^+ more efficiently is expected to facilitate axonal
231 resilience to high frequency spiking. Existing data argue that Na^+ removal after spiking is slow. In
232 axon initial segments of L5 pyramidal neurons, as a result of Na^+ diffusing into the soma and
233 myelin wrapped compartments, elevated [Na^+] requires several seconds to approximately recover
234 (16). In mitral cell tuft dendrites, after a short period of high frequency stimulation, it takes minutes
235 for the Na/K ATPase to pump out the accumulated Na^+ (17). This slow Na^+ removal may be
236 functionally important because it enables integration and binding of multiple chemosensory stimuli
237 over a prolonged time scale (40). We used pump densities that should fall into a reasonable
238 biological range, and the Na^+ accumulation at high firing frequencies shown here is consistent with
239 recent Na^+ imaging data (17, 20).

240 This work illustrates the limitations of using conventional frequency-current curves generated
241 with a short-term current injection to estimate the reliability of spike propagation (41, 42). Neither
242 of these measures reflects the accommodation of neuronal excitability after continuous firing
243 caused changes such as Na^+ (explored in this work) and Ca^{2+} accumulation (showing a biphasic
244 decay (43, 44)).

245 In the models explored here, myelinated axons are resilient to high frequency spiking elicited
246 Na^+ accumulation. Given that myelinated axons are usually much thicker (1, 45), spike propagation
247 in myelinated axons should be extremely robust to fast spiking caused Na^+ accumulation under
248 usual physiological conditions. However, under conditions requiring neurons to fire for extended
249 time at high frequencies, Na^+ accumulation may still compromise the function of axons. Of course,
250 the frequency threshold and the number of spikes required to cause spike failure will depend on
251 the specifics of the expression of neuronal conductances, and will likely show variability as a
252 consequence of variable channel densities (46). Additionally, intrinsic channel noise can cause

253 spike failure (4, 27), and the normal function of the Na/K ATPases requires ATP, the supply of
254 which has a limit (35). Both a shortage of ATP after continuous firing and channel noise can further
255 reduce axonal reliability of propagating spikes.

256 In recent years, a trade-off has been proposed between a neuron's capability to spike rapidly
257 and the high energetic cost of spiking (8, 47). To achieve high spike rates (narrow spikes), neurons
258 need to consume more energy to remove the larger Na^+ influx, coproduct of fast spiking. However,
259 in our simulations, we find a more complicated relationship between Na^+ influx and spike duration
260 (Fig. 4). Furthermore, although narrow spikes can facilitate high frequency spike generation, they
261 are more vulnerable to Na^+ accumulation or noise disturbance during propagation. This work
262 implies that different strategies may be required in different types of neurons to guarantee reliable
263 spike propagation for their functional requirements.

264 Materials and Methods

265 **Axonal Morphology.** We modeled a segment of axon with the length of 3131 μm. The model was
266 implemented in NEURON (23). The model code is available from ModelDB (accession number:
267 267009). The simulations used an integration step of 0.05 ms. The unmyelinated model was
268 discretized into 51 segments in the longitudinal direction. For the myelinated axon model, there
269 are 31 nodes of Ranvier flanked with 32 myelinated compartments (Figure 1). The lengths of the
270 nodes of Ranvier are 1 μm (nseg = 1). Each myelinated compartment is 100 μm long (nseg = 3),
271 except the outer two myelinated compartments are 50 μm each (nseg = 3). In the radial direction,
272 there are 4 shells to model Na^+ diffusion (23). The Na^+ diffusion coefficient is 0.6 $\mu m^2/ms$ (24)
273 and there is no buffering (16), leading to a homogeneous $[Na^+]$ in the radial direction. In both
274 peripheral and central nervous systems, unmyelinated axons are usually thinner than myelinated

275 axons. In the central nervous system, axons > 0.2 μm are usually myelinated (1). To delineate the
276 effect of both diameter and myelination on Na^+ accumulation, we chose the same range of
277 diameters between 0.2–1.0 μm.

278 **Ionic Channels and the Na/K pump.** The model has a minimal set of ionic channels: fast Na
279 current (I_{Na}), delayed rectifier K current (I_{KD}), A-type K current (I_{KA}) and leak current (I_{leak}). They
280 have standard kinetic formulations in the form of $I = g_{max} m^p h^q (V - E)$; $\tau_m \dot{m} = m_\infty(V) -$
281 m; $\tau_h \dot{h} = h_\infty(V) - h$; g_{max} represents maximal conductance; m and h represent activation and
282 inactivation gates; p and q represent corresponding gate exponents; E represents equilibrium
283 potential; τ_m and τ_h represent corresponding time constants; All the channel kinetics were
284 modified from (48). For I_{Na}, $g_{max} = 0.015\, S/cm^2$; $p = 3$; $q = 1$; $m_\infty =$
285 $1/(1 + exp(-(V + 38)/8.5))$; $\tau_m = 0.132/(\cosh((V + 27)/7.5) + 0.003/(1 +$
286 $\exp(-(V + 27)/5)))$; $h_\infty = 1/(1 + exp(V + 47/6))$; $\tau_h = 10/cosh((V + 42)/15)$; $E_{Na} =$
287 $RT/F * \ln([Na^+]_o/[Na^+]_i)$; $[Na^+]_o$ is fixed to be 140 mM; $[Na^+]_i$ (also written as $[Na^+]$ in the
288 main text) was dynamically computed by I_{Na} and the Na/K pump; For I_{KD}, $g_{max} = 0.216\, S/cm^2$;
289 $p = 4$; $q = 0$; $m_\infty = (-0.01 * (V + 45.7)/(exp(-(V + 45.7)/10) - 1))/((-0.01 * (V +$
290 $45.7)/(exp(-(V + 45.7)/10) - 1)) + 0.125 * exp(-(V + 55.7)/80))$; $\tau_m = 1/((-0.01 *$
291 $(V + 45.7)/(exp(-(V + 45.7)/10) - 1)) + 0.125 * exp(-(V + 55.7)/80))$; E_K = -70 mV;
292 For I_{KA}, $g_{max} = 0.02\, S/cm^2$; $p = 3$; $q = 1$; $m_\infty = (0.0761 * exp((V + 94.22)/31.84)/(1 +$
293 $exp((V + 1.17)/28.93)))^{1/3}$; $\tau_m = 0.3632 + 1.158/(1 + exp((V + 55.96)/20.12))$; $h_\infty =$
294 $1/\left(1 + exp(V + 53.3/14.54)\right)^4$; $\tau_h = 1.24 + 2.678/(1 + exp((V + 50)/16.027))$; For
295 I_{leak}, $g_{max} = 1.25 \times 10^{-4}\, S/cm^2$; $p = 0$; $q = 0$; E_{leak} = -65 mV; the Na/K pump model is
296 similar with that used in (17, 40), described by the following kinetic schemes: $[pump] + 3[Na^+]_i$

$\overset{k_1,k_2}{\longleftrightarrow}[pumpNa]$; $[pumpNa] \overset{k_3,k_4}{\longleftrightarrow}[pump] + 3[Na^+]_o$; $pump_{total} = [pump] + [pumpNa]$; $k_1 = 2\ mM^{-3}msec^{-1}$; $k_2 = 0.001\ msec^{-1}$; $k_3 = 0.6\ msec^{-1}$; $k_4 = 0.437\ mM^{-3}msec^{-1}$; By these parameters, the steady state $[Na^+]$ is ~ 10 mM when the axon models are silent. For Fig. 4, a scaling factor in the range of 0.2 -1.4 was multiplied with τ_m at all voltages for I_{KD}.

For the unmyelinated axon model, all defined currents and the Na/K pump were evenly distributed with C_m = 1 μF/cm^2 and R_a = 120 Ωcm. For the myelinated axon model, the ionic currents and the Na/K pump were placed in the nodes of Ranvier (1, 49). For simplicity, we did not model juxtaparanodal regions. At the nodes of Ranvier, C_m = 1 μF/cm^2; On myelinated compartments, there is only a smaller I_{leak} with g_{max} = 1.25×10^{-6} S/cm^2 and effective C_m = 0.01 μF/cm^2; R_a is 120 Ωcm. In both the unmyelinated and the myelinated axon models, the current densities are identical so that we could explore the role of diameter and myelination on Na^+ accumulation. The $pump_{total}$ is in the range of 0.5–5 pmol/cm^2. We did not explicitly simulate the axon initial segment in our model. Instead, we applied strong enough current at the starting end of the unmyelinated model and the first node of Ranvier in the myelinated model to reliably trigger spikes.

Acknowledgments

The authors would like to thank the constructive suggestions from the reviewers and from the members of Marder lab. This work was supported by the grant R35NS097343.

References

1. S. G. Waxman, J. D. Kocsis, P. K. Stys, *The Axon: Structure, Function, and Pathophysiology* (Oxford University Press, 1995).
2. D. Debanne, E. Campanac, A. Bialowas, E. Carlier, G. Alcaraz, Axon physiology. Physiol Rev **91**, 555-602 (2011).
3. H. Schmidt, T. R. Knosche, Action potential propagation and synchronisation in myelinated axons. PLoS Comput Biol **15**, e1007004 (2019).

322 4. A. A. Faisal, J. A. White, S. B. Laughlin, Ion-channel noise places limits on the
323 miniaturization of the brain's wiring. Curr Biol **15**, 1143-1149 (2005).
324 5. J. A. Perge, J. E. Niven, E. Mugnaini, V. Balasubramanian, P. Sterling, Why do axons differ
325 in caliber? J Neurosci **32**, 626-638 (2012).
326 6. B. Wang *et al.*, Firing Frequency Maxima of Fast-Spiking Neurons in Human, Monkey, and
327 Mouse Neocortex. Front Cell Neurosci **10**, 239 (2016).
328 7. S. Chen, G. J. Augustine, P. Chadderton, Serial processing of kinematic signals by
329 cerebellar circuitry during voluntary whisking. Nat Commun **8**, 232 (2017).
330 8. A. Hasenstaub, S. Otte, E. Callaway, T. J. Sejnowski, Metabolic cost as a unifying principle
331 governing neuronal biophysics. Proc Natl Acad Sci USA **107**, 12329-12334 (2010).
332 9. S. B. Laughlin, Energy as a constraint on the coding and processing of sensory information.
333 Curr Opin Neurobiol **11**, 475-480 (2001).
334 10. W. B. Levy, R. A. Baxter, Energy efficient neural codes. Neural Comput **8**, 531-543 (1996).
335 11. H. Alle, A. Roth, J. R. Geiger, Energy-efficient action potentials in hippocampal mossy
336 fibers. Science **325**, 1405-1408 (2009).
337 12. F. J. Heras, J. Anderson, S. B. Laughlin, J. E. Niven, Voltage-dependent K^+ channels improve
338 the energy efficiency of signalling in blowfly photoreceptors. J R Soc Interface **14** (2017).
339 13. H. Hu, F. C. Roth, D. Vandael, P. Jonas, Complementary Tuning of Na^+ and K^+ Channel
340 Gating Underlies Fast and Energy-Efficient Action Potentials in GABAergic Interneuron
341 Axons. Neuron **98**, 156-165 e156 (2018).
342 14. C. Howarth, P. Gleeson, D. Attwell, Updated energy budgets for neural computation in
343 the neocortex and cerebellum. J Cereb Blood Flow Metab **32**, 1222-1232 (2012).
344 15. R. Nortley, D. Attwell, Control of brain energy supply by astrocytes. Curr Opin Neurobiol
345 **47**, 80-85 (2017).
346 16. I. A. Fleidervish, N. Lasser-Ross, M. J. Gutnick, W. N. Ross, Na^+ imaging reveals little
347 difference in action potential-evoked Na^+ influx between axon and soma. Nat Neurosci
348 **13**, 852-860 (2010).
349 17. A. Zylbertal, A. Kahan, Y. Ben-Shaul, Y. Yarom, S. Wagner, Prolonged Intracellular Na^+
350 Dynamics Govern Electrical Activity in Accessory Olfactory Bulb Mitral Cells. PLoS Biol **13**,
351 e1002319 (2015).
352 18. A. Zylbertal, Y. Yarom, S. Wagner, The Slow Dynamics of Intracellular Sodium
353 Concentration Increase the Time Window of Neuronal Integration: A Simulation Study.
354 Front Comput Neurosci **11**, 85 (2017).
355 19. D. Ziemens, F. Oschmann, N. J. Gerkau, C. R. Rose, Heterogeneity of Activity-Induced
356 Sodium Transients between Astrocytes of the Mouse Hippocampus and Neocortex:
357 Mechanisms and Consequences. J Neurosci **39**, 2620-2634 (2019).
358 20. T. Ona-Jodar, N. J. Gerkau, S. Sara Aghvami, C. R. Rose, V. Egger, Two-Photon Na^+ Imaging
359 Reports Somatically Evoked Action Potentials in Rat Olfactory Bulb Mitral and Granule Cell
360 Neurites. Front Cell Neurosci **11**, 50 (2017).
361 21. B. Moshrefi-Ravasdjani, D. Ziemens, N. Pape, M. Färfers, C. R. Rose, Action Potential Firing
362 Induces Sodium Transients in Macroglial Cells of the Mouse Corpus Callosum. Neuroglia
363 **1**, 106-125 (2018).

364 22. Y. Zang *et al.*, Theoretical investigation of the mechanism of heart failure using a canine
365 ventricular cell model: especially the role of up-regulated CaMKII and SR Ca^{2+} leak. J Mol
366 Cell Cardiol **56**, 34-43 (2013).
367 23. M. L. Hines, N. T. Carnevale, The NEURON simulation environment. Neural Comput **9**,
368 1179-1209 (1997).
369 24. M. J. Kushmerick, R. J. Podolsky, Ionic mobility in muscle cells. Science **166**, 1297-1298
370 (1969).
371 25. L. S. Tang *et al.*, Precise temperature compensation of phase in a rhythmic motor pattern.
372 PLoS Biol **8**, e1000469 (2010).
373 26. J. C. Athilingam, R. Ben-Shalom, C. M. Keeshen, V. S. Sohal, K. J. Bender, Serotonin
374 enhances excitability and gamma frequency temporal integration in mouse prefrontal
375 fast-spiking interneurons. Elife **6**, e31991 (2017).
376 27. D. Al-Basha, S. A. Prescott, Intermittent Failure of Spike Propagation in Primary Afferent
377 Neurons during Tactile Stimulation. J Neurosci **39**, 9927-9939 (2019).
378 28. M. D. Forrest, The sodium-potassium pump is an information processing element in brain
379 computation. Frontiers in Physiology **5** (2014).
380 29. L. R. Shao, R. Janicot, C. E. Stafstrom, Na^+-K^+-ATPase functions in the developing
381 hippocampus: regional differences in CA1 and CA3 neuronal excitability and role in
382 epileptiform network bursting. J Neurophysiol **125**, 1-11 (2021).
383 30. D. Kueh, W. H. Barnett, G. S. Cymbalyuk, R. L. Calabrese, Na^+/K^+ pump interacts with the
384 h-current to control bursting activity in central pattern generator neurons of leeches. Elife
385 **5**, e19322 (2016).
386 31. M. D. Forrest, M. J. Wall, D. A. Press, J. Feng, The sodium-potassium pump controls the
387 intrinsic firing of the cerebellar Purkinje neuron. PLoS One **7**, e51169 (2012).
388 32. A. O. Komendantov, C. C. Canavier, Electrical coupling between model midbrain
389 dopamine neurons: effects on firing pattern and synchrony. J Neurophysiol **87**, 1526-1541
390 (2002).
391 33. C. C. Canavier, Sodium dynamics underlying burst firing and putative mechanisms for the
392 regulation of the firing pattern in midbrain dopamine neurons: a computational approach.
393 J Comput Neurosci **6**, 49-69 (1999).
394 34. G. P. Krishnan, G. Filatov, A. Shilnikov, M. Bazhenov, Electrogenic properties of the Na^+/K^+
395 ATPase control transitions between normal and pathological brain states. J Neurophysiol
396 **113**, 3356-3374 (2015).
397 35. G. Le Masson, S. Przedborski, L. F. Abbott, A computational model of motor neuron
398 degeneration. Neuron **83**, 975-988 (2014).
399 36. J. S. Coggan, G. K. Ocker, T. J. Sejnowski, S. A. Prescott, Explaining pathological changes in
400 axonal excitability through dynamical analysis of conductance-based models. J Neural Eng
401 **8**, 065002 (2011).
402 37. N. Yu, C. E. Morris, B. Joos, A. Longtin, Spontaneous excitation patterns computed for
403 axons with injury-like impairments of sodium channels and Na/K pumps. PLoS Comput
404 Biol **8**, e1002664 (2012).
405 38. J. Stedehouder *et al.*, Fast-spiking Parvalbumin Interneurons are Frequently Myelinated
406 in the Cerebral Cortex of Mice and Humans. Cereb Cortex **27**, 5001-5013 (2017).

407 39. N. Doyon *et al.*, Efficacy of synaptic inhibition depends on multiple, dynamically
408 interacting mechanisms implicated in chloride homeostasis. PLoS Comput Biol **7**,
409 e1002149 (2011).
410 40. A. Zylbertal, Y. Yarom, S. Wagner, Synchronous Infra-Slow Bursting in the Mouse
411 Accessory Olfactory Bulb Emerge from Interplay between Intrinsic Neuronal Dynamics
412 and Network Connectivity. J Neurosci **37**, 2656-2672 (2017).
413 41. N. W. Gouwens *et al.*, Classification of electrophysiological and morphological neuron
414 types in the mouse visual cortex. Nat Neurosci **22**, 1182-1195 (2019).
415 42. A. Foust, M. Popovic, D. Zecevic, D. A. McCormick, Action Potentials Initiate in the Axon
416 Initial Segment and Propagate through Axon Collaterals Reliably in Cerebellar Purkinje
417 Neurons. The Journal of Neuroscience **30**, 6891-6902 (2010).
418 43. H. Schmidt, K. M. Stiefel, P. Racay, B. Schwaller, J. Eilers, Mutational analysis of dendritic
419 Ca^{2+} kinetics in rodent Purkinje cells: role of parvalbumin and calbindin D28k. J Physiol
420 **551**, 13-32 (2003).
421 44. Y. Zang, S. Dieudonne, E. De Schutter, Voltage- and Branch-Specific Climbing Fiber
422 Responses in Purkinje Cells. Cell Rep **24**, 1536-1549 (2018).
423 45. S. Lee *et al.*, A culture system to study oligodendrocyte myelination processes using
424 engineered nanofibers. Nat Methods **9**, 917-922 (2012).
425 46. D. J. Schulz, J. M. Goaillard, E. Marder, Variable channel expression in identified single and
426 electrically coupled neurons in different animals. Nat Neurosci **9**, 356-362 (2006).
427 47. B. C. Carter, B. P. Bean, Sodium entry during action potentials of mammalian neurons:
428 incomplete inactivation and reduced metabolic efficiency in fast-spiking neurons. Neuron
429 **64**, 898-909 (2009).
430 48. Y. Zhang, D. Bucher, F. Nadim, Ionic mechanisms underlying history-dependence of
431 conduction delay in an unmyelinated axon. Elife **6**, e25382 (2017).
432 49. S. G. Waxman, J. M. Ritchie, Molecular dissection of the myelinated axon. Ann Neurol **33**,
433 121-136 (1993).
434

435

Figures and Tables

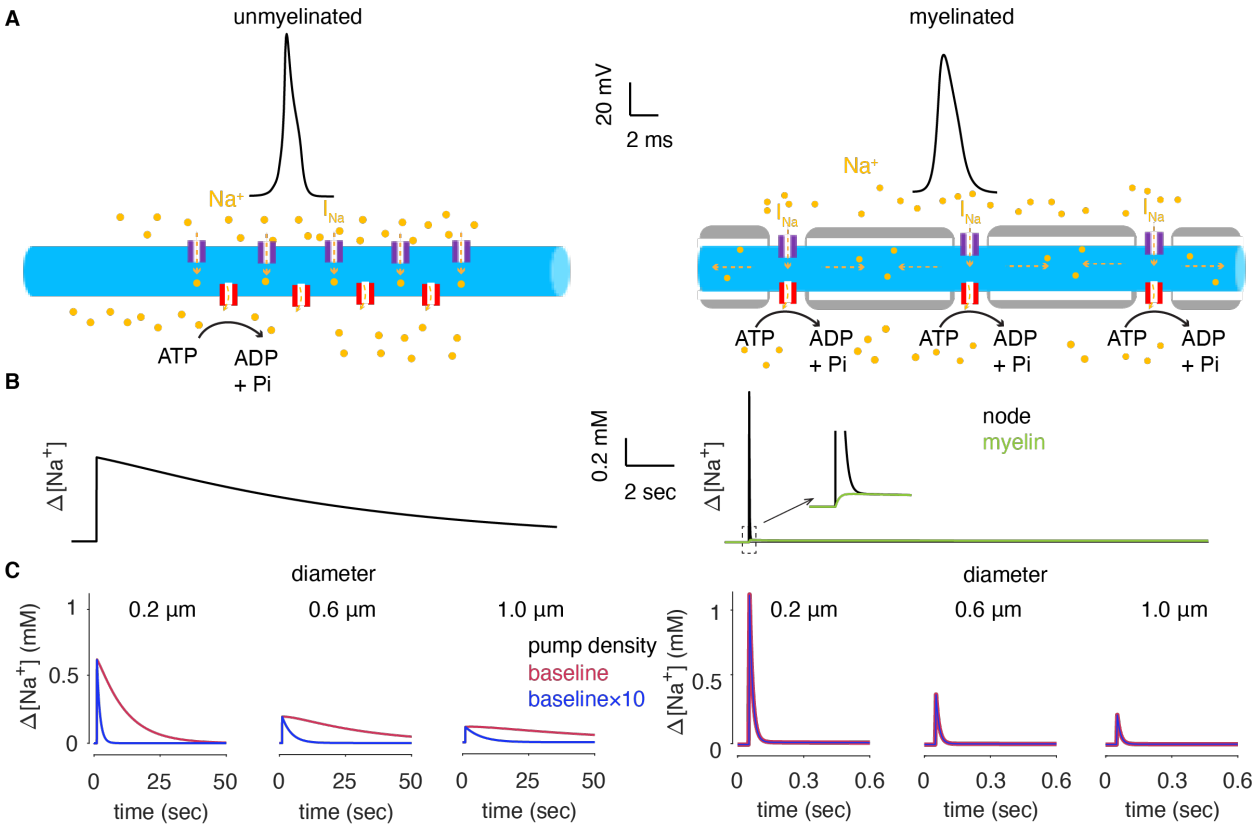

Figure 1. Spike-triggered [Na^+] rise and decay in unmyelinated and myelinated axon models. (A) Schematics of the unmyelinated (left) and the myelinated (right) axon models. Black traces show spike waveforms in two models (50 µm from the distal axon end; In myelinated model, it is also a node of Ranvier). (B) Spike-triggered [Na^+] rise and decay in the unmyelinated (left) and the myelinated (right) axon models. Black traces were measured at corresponding voltage recording sites. Green trace shows [Na^+] in the myelinated compartment (16.7 µm from the node of Ranvier) and the initial part is enlarged in the inset. The Na/K pump density is 0.5 pmol/cm^2, referred to as baseline condition hereafter. (C) The effects of diameter and pump density on [Na^+] rise and decay in the unmyelinated (left) and the myelinated (right, at the node of Ranvier) axon models. Note the very different time scales in the two models.

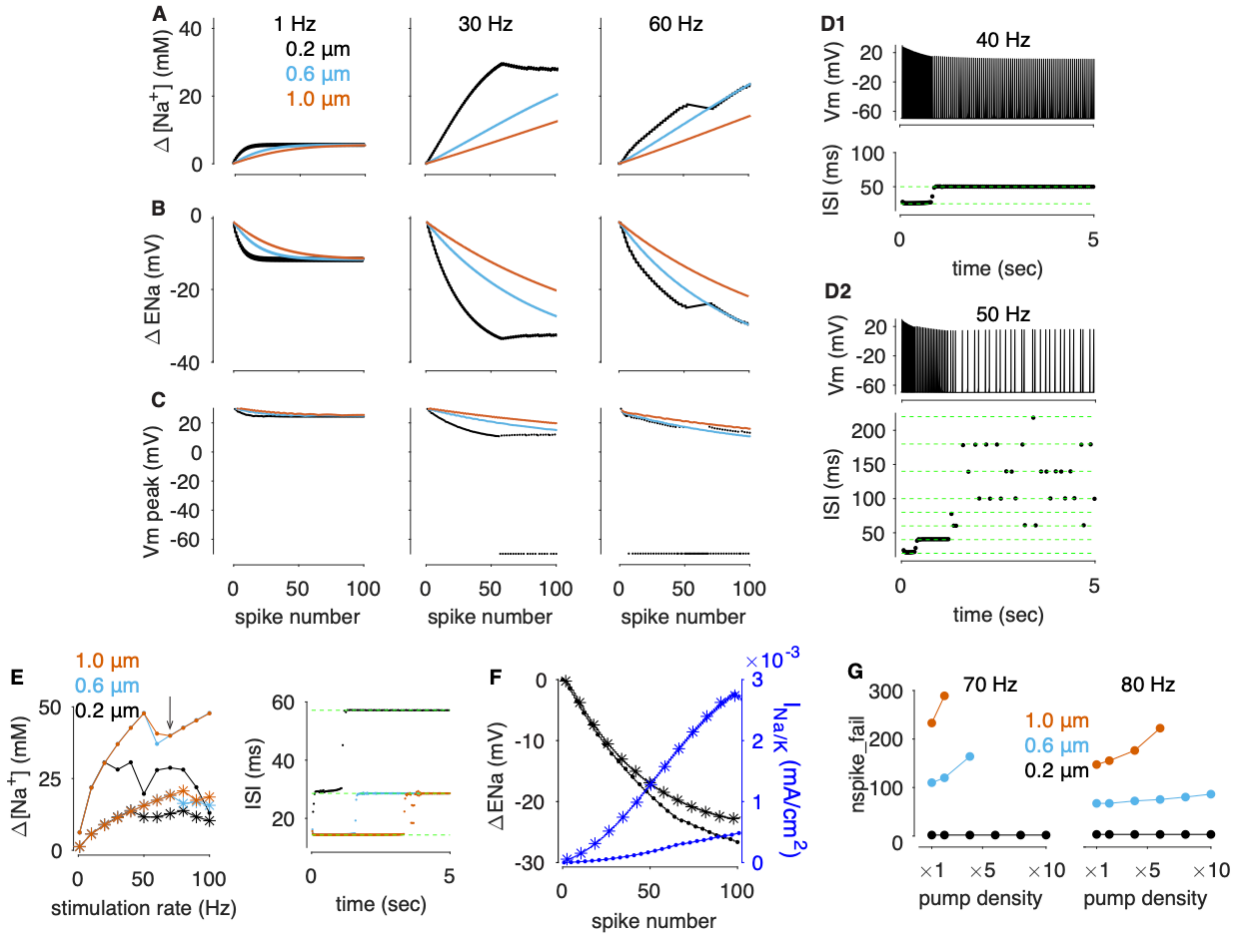

Figure 2. The effects of diameter and pump density on Na^+ accumulation and resilience to high frequency spiking in the unmyelinated axon model. A-C show $[Na^+]$ increase, Na^+ equilibrium potential decrease and membrane potential peak reduction (bottom) in models with different diameters and firing frequencies. (D) Voltage traces and interspike intervals (ISIs) at distal axon for 40 Hz (D1) and 50 Hz (D2) spike signals in the 0.2-µm-diameter axon. (E) Steady state $[Na^+]$ elevation at different stimulation frequencies (left). Right panel shows ISIs at distal axon for 70 Hz spike signals with baseline pump density. (F) Na^+ equilibrium potential decrease (black) and outward pump current increase (blue) with different pump densities. 80 Hz spike signals in the 0.6-µm-diameter axon. In E & F, dot and star represent 1 and 10 times of baseline pump density, respectively. (G) The effect of pump density on axonal resilience to high frequency spiking, measured by the number of spikes required to cause propagation failure (nspike_fail), when firing at 70 and 80 Hz. The absence of data points means propagation doesn't fail under corresponding conditions.

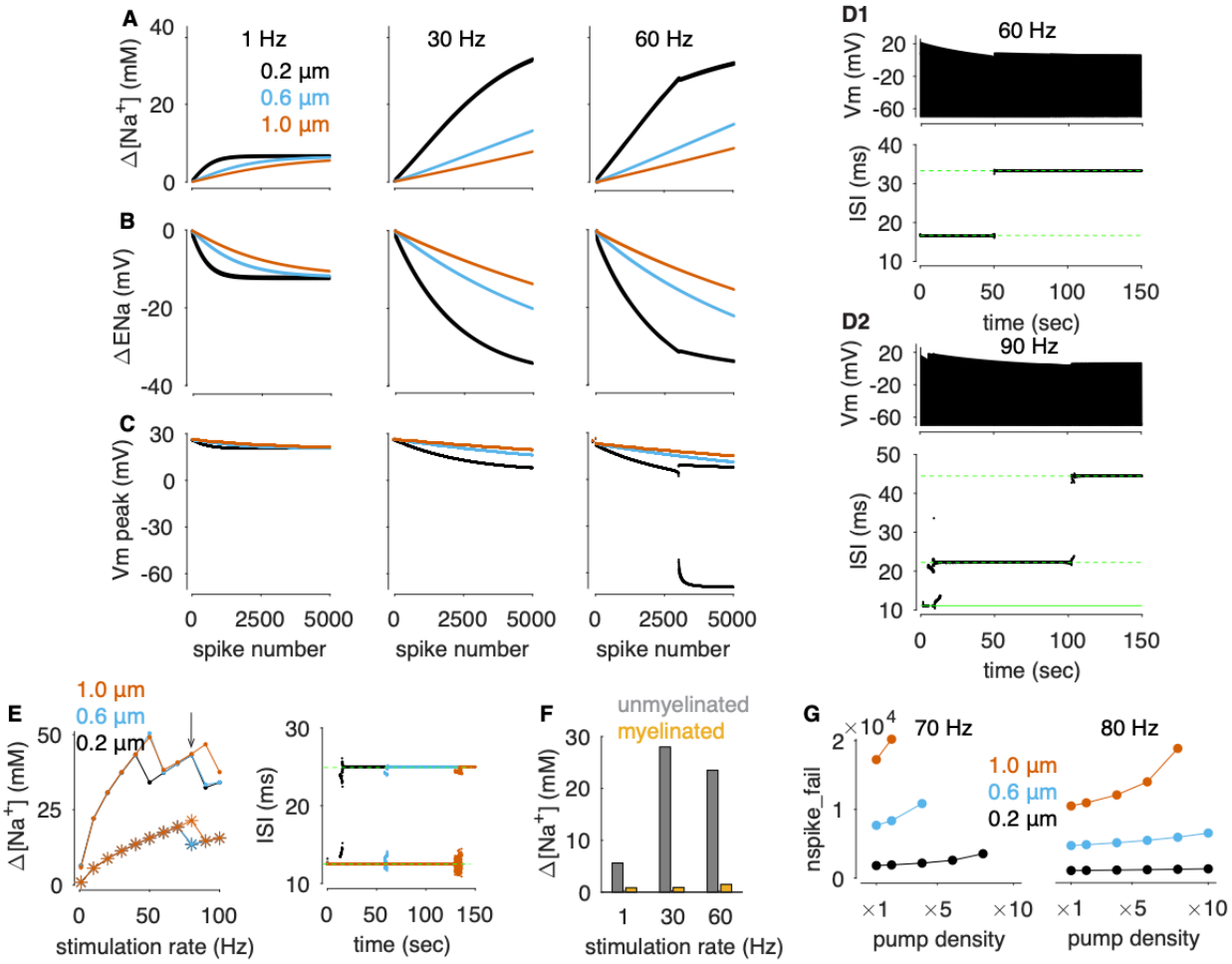

Figure 3. Myelination slows Na^+ accumulation to increase axonal resilience to high frequency spiking. A-C show $[Na^+]$ increase, Na^+ equilibrium potential decrease and membrane potential peak reduction at the node of Ranvier in the myelinated axon model with different diameters and firing frequencies. (D) Voltage traces and ISIs at distal axon for 60 Hz (D1) and 90 Hz (D2) spike signals in the 0.2-µm-diameter axon. (E) Steady state $[Na^+]$ elevation at different stimulation frequencies (left). Dot and star represent 1 and 10 times of baseline pump density, respectively. Right panel shows ISIs at distal axon for 80 Hz spike signals with baseline pump density. (F) 100-spike caused Na^+ accumulation in the unmyelinated axon and the myelinated axon (node of Ranvier). The diameter is 0.2 µm, with baseline pump density. (G) The effect of pump density on axonal resilience to high frequency spiking, when firing at 70 Hz and 80 Hz. The absence of data points means propagation doesn't fail under corresponding conditions.

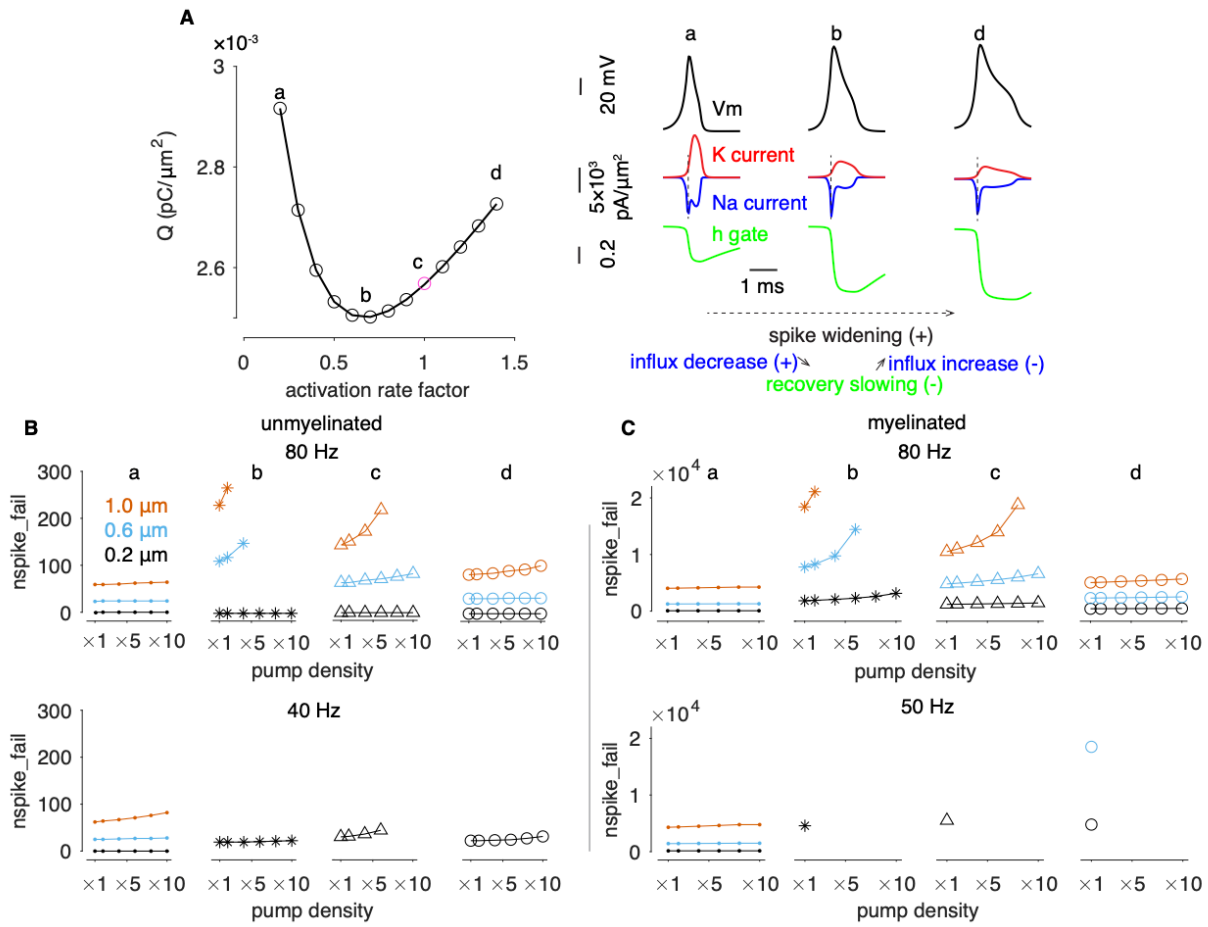

Figure 4. Complex effects of slowing I_{KD} activation on Na^+ influx rate and propagation resilience. (A) U-shaped dependence between Na^+ influx rate and I_{KD} activation rate. y axis (left panel) measures single spike triggered Na^+ influx per μm^2. c represents the baseline model (magenta); a, b and d represent 0.2, 0.6 and 1.4 times of the baseline I_{KD} activation time constant, respectively. Changes of spike shape, current profile and Na^+ channel inactivation gate state with slowed I_{KD} activation. The effects of delayed activation of I_{KD} on propagation resilience in unmyelinated and myelinated models are shown in B and C, respectively. a - d correspond to conditions defined in A. Resilience changes are measured by comparing symbols of the same color (coding diameter). For example, from a to b at 40 Hz in the unmyelinated model, black stars are higher than black dots, suggesting increased resilience in the 0.2-µm-diameter axon. The resilience also increases in larger diameter axons, because slowed I_{KD} activation eliminates propagation failure. The absence of data points means propagation doesn't fail under corresponding conditions.

Supporting Information

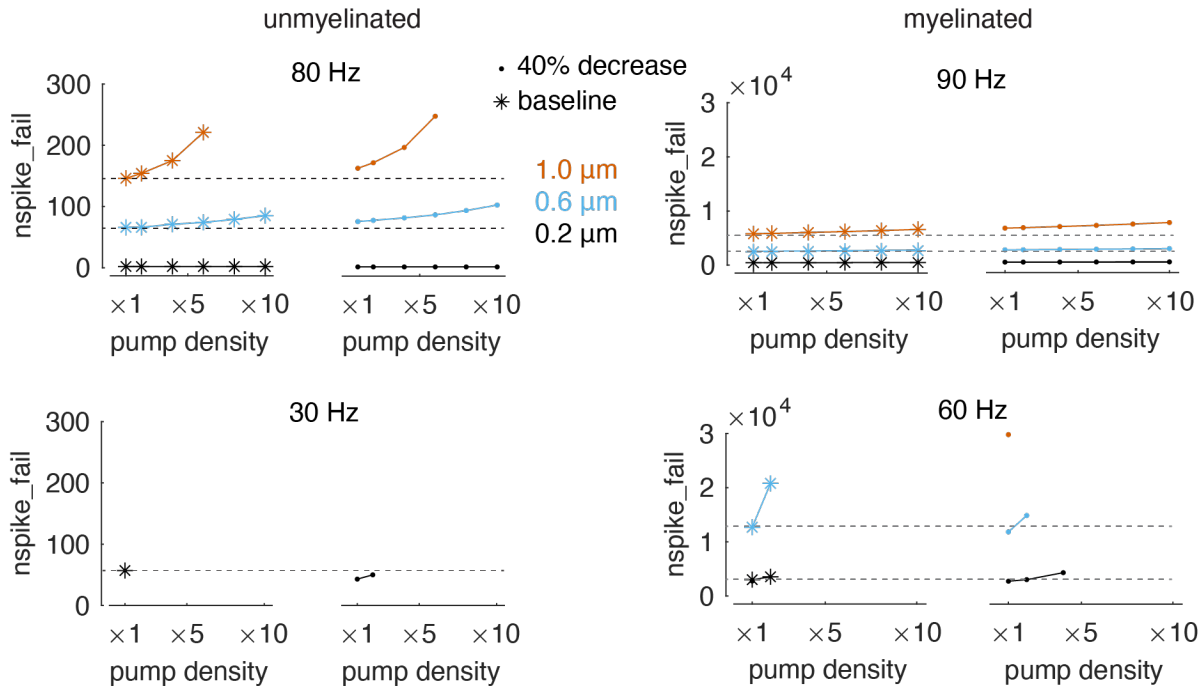

Figure S1. The effects of increasing the rate of Na^+ current inactivation on propagation resilience. Star represents the baseline model and dot represents 40% decreased inactivation time constant of Na^+ current. In unmyelinated axon models, at 30 Hz, faster inactivation decreases the resilience in the 0.2-µm-diameter axon model (dots are lower than stars). At 80 Hz, faster inactivation increases the resilience (dots are higher than stars). The same trend is observed in myelinated axon models. The absence of data points means propagation doesn't fail.